

## SUPPLEMENTARY INFORMATION

### An effective Fe(II) doping strategy for stable and highly photoluminescent CsPbBr<sub>2</sub> nanocrystals

Yanbin Chen,<sup>a</sup> Hwei Yang,<sup>b</sup> Jian Song<sup>\*a</sup> and Bao Zhang<sup>\*a</sup>

*a. School of Chemical Engineering and Technology, Tianjin University, Tianjin, 300350, China.*

*Email: baozhang@tju.edu.cn, songjian@tju.edu.cn*

*b. Institute of Chemical Materials, China Academy of Engineering Physics, Mianyang 621900, China.*

### Supplementary Discussion

#### Section 1

Herein, the experimental details related to Br-2 were discussed. During the purification process, it was found difficult to precipitate NCs from the crude solution only by increasing the rotation speed or prolonging the centrifugation time. Hence, the commonly used antisolvent ethyl acetate (EA) was added to the crude solution to precipitate NCs (See Experimental Section 2.5 for details). However, only a small number of PNCs was obtained, indicating that excessive iron precursors would decrease the yield of PNCs. Furthermore, ICP-MS showed that the actual Fe/Pb ratio of Br-2 was 2.7%, which was merely slightly higher than the Br-2.4%. The slight change in Fe<sup>2+</sup> content, although not confirmed so far, was suspected to be the result of the self-purification effect,<sup>1</sup> which excluded excess Fe<sup>2+</sup> within lattice and thus controlled the Fe<sup>2+</sup> content at a low level.

The crystal information of Br-2 was also studied by XRD as shown in Fig. S5. Compared with Br-2.4%, both the (100) and (200) XRD peaks for Br-2 shifted to higher 2θ, implying that further lattice contraction occurred. The broadening of the diffraction peak for Br-2 indicated the reduction in grain size, as confirmed by TEM image (Fig. S6a). Meanwhile, splitting of (200) XRD peak implied the existence of microstrain in the crystal,<sup>2,3</sup> suggesting that a large amount of Fe<sup>2+</sup> would reduce the symmetry of the cubic phase.

The XPS results of Br-2 revealed a Pb/X ratio of 1:2.484, indicating the increased content of crystal defects, which could be attributed to the destruction by ODE-EA system (discussed in Section 2) and lattice distortion induced by excessive Fe<sup>2+</sup> doping. With the aid of the surface etching caused by ODE-EA system, the otherwise undetectable Fe signal was observed (Fig. S7f), indicating that Fe<sup>2+</sup> was mainly distributed within the lattice instead of the surface of PNCs. In the HR-XPS spectra, the binding energies for Pb 4f, Br 3d, I 3d in Br-2 shifted to higher binding values (Fig. S7b-7d), which is consistent with the further contraction evidenced by XRD results. Interestingly, the binding energies for Cs 3d also increased in Br-2 (Fig. S7e), although Cs<sup>+</sup> was not considered to interact directly with Pb<sup>2+</sup>/Fe<sup>2+</sup>. As we explained in Section 2, the ODE-EA system would increase the Br/I ratio, resulting in the increased average electronegativity of halides, and thus the Cs-X interaction was modified.

Furthermore, the Br-2 maintained orange emission at 630 nm, with PLQY of 59.8% (Fig. S8). The decline of PLQY may be attributed to the formation of defects resulted from the surface etching and lattice distortion induced by excessive Fe<sup>2+</sup> doping.

As discussed above, the structure and luminescence properties of Br-2 and Br-2.4% showed significant differences. Apart from the difference in dopant concentration, the purification process of Br-2 and Br-2.4% were different. Hence, we also investigated the influence of the purification method, and a surface etching process caused by octadecene (ODE) and EA was conceived, as shown in Fig. S9 (See Supplementary Discussion Section 2 for studies).

## Section 2

As a commonly used antisolvent, it is known that EA could promote the separation of NCs from unreacted precursors and ODE, while increasing the product yield during purification. However, an excessive amount of antisolvent will cause agglomeration or redissolution of perovskite, destroying the crystal structure. Besides, the damaging effect of solvent ODE on CsPbX<sub>3</sub>, especially CsPbI<sub>3</sub>, have been reported.<sup>4,5</sup> By adding a mixture of ODE and EA to the dispersion of CsPbBrI<sub>2</sub> NCs in hexane, we observed the dramatic PL degradation process, confirming the destructive effect of ODE and EA on CsPbBrI<sub>2</sub> (Fig. S10). Herein, the influence of ODE and antisolvent EA on the structure and performance of PNCs was investigated.

To compare the differences between centrifugation method 1 and 2, a set of samples were obtained using centrifugation method 2, labeled Pri-EA, Br-EA, Ac-EA, and F-EA, collectively referred to as PNC-EA. The structure and luminescence performance of PNCs were carefully studied by using TEM, XRD, PL, TRPL measurements. It was found that, compared to their counterparts, PNC-EA retained a smaller average particle size, ranging from 11.3-15.2 nm (Fig. S11 and Fig. S12). We speculated that the mixture of ODE and EA would show the etching effect on the surface of CsPbBrI<sub>2</sub> NCs, resulting in the reduction of particle size. XRD patterns indicated that, compared with undoped CsPbBrI<sub>2</sub> NCs, the signals of (100) and (200) planes in Pri-EA were significantly weakened (Fig. S13), indicating that the crystallinity of corresponding planes became worse. We also observed the broadening of the characteristic diffraction peaks of Pri-EA, which could be attributed to the grain refinement as evidenced by TEM image. In addition, the XRD spectrum of the Pri-EA film showed random orientation of the powder characteristics, indicating that the assembly method between NCs and Si substrate had changed.<sup>6,7</sup> These data indicated that the crystal structure of PNCs was changed during purification process. Furthermore, the additional diffraction peaks attributed to CsI and CsOH indicated that PNCs had undergone a humidity-induced decomposition process.<sup>8</sup>

The PL spectrum showed that the PL peak of PNC-EA exhibited a blueshift of 5-19 nm compared to their counterparts (Fig. S14a and Table S4). It is reported that adding the antisolvent isopropanol to the crude solution of CsPbBr<sub>3</sub> NCs would cause the agglomeration, resulting in a redshift of the PL emission peak.<sup>6</sup> In our experiments, the existence of surface ligands in PNC-EA maintained the existence of NCs (Fig. S3). To figure out the cause of the PL peak shift, the contribution of quantum confinement effects to band gap was estimated using Equation 1. The decreased average size of Pri-EA from 20.2 to 14.1 nm would result a reduction of band gap  $\sim 4.8 \times 10^{-3}$  eV. The mismatch between calculated value and observed PL emission peak shift indicated the existence of other factors that caused the band gap to decrease. Based on the high angle shift of XRD diffraction peaks and the decreased lattice constant in HR-TEM (Fig. S11 and Fig. S13), we considered that the etching process caused by ODE and EA changed the halide composition of PNCs, which contributes to the increase of band gap. The weaker interactions between I<sup>-</sup> and oleylammonium / Pb<sup>2+</sup> made the iodide components more vulnerable compared to

the cases in bromide components,<sup>5,6</sup> resulting in the increased Br/I ratio after purification. The PLQYs and PL lifetimes were shown in Fig. S14b and 14c and Table S4. The decreased PL lifetimes could be attributed to the increased exciton binding energy induced by the increased Br/I ratio and decreased particle size. In addition, it was found that  $K_r$  did not change significantly but  $K_{nr}$  increased significantly in PNC-EA, indicating that a large number of defects were generated during the etching process, which accelerated the nonradiative recombination rate and resulted in decreased PLQYs.

The above results disclosed the changes in structure and luminescence performance of CsPbBr<sub>2</sub> NCs with and without etching and provided support for our understanding of this process. The CsPbX<sub>3</sub> perovskites were endowed with the properties of the large ionic mobilities within the lattice and dynamic surface. Nonetheless, the ion exchange process becomes slow and uneven in systems with high viscosity, such as gels.<sup>9</sup> This novel phenomenon inspired us to understand the observed experimental phenomena. In the hexane-EA system, despite the ligand desorption process, the rapid ligand resorption process makes the exposed surface passivated in time. Nevertheless, both processes were greatly slowed down in ODE-EA system due to the relatively high viscosity of ODE, resulting in the exposure of the NCs surface. The exposed surface of CsPbBr<sub>2</sub> was destroyed by ODE and EA, resulting in structure collapse, which caused changes in crystal structure and luminescence properties. In both systems, the antisolvent EA weakens the binding strength between ligands and perovskite and promotes the ligand desorption process, leading to the production of Cs-oleate, X-oleylammonium or Pb-oleate species.<sup>4-6</sup>

The structure and performance changes of CsPbBr<sub>2</sub> NCs in the ODE-EA system reflect its lattice instability, which is related to the intrinsic ionic nature of perovskite. We have summarized the variations of average particle size, PL peak position and PLQYs of samples obtained using centrifugation methods 1 and 2, as shown in Table S5. We found that Fe<sup>2+</sup> doped PNCs is affected much weaker than undoped sample, which implies the higher lattice stability of Fe<sup>2+</sup> doped samples against ODE and EA.

As far as we know, pyridine etching and ion gun etching have been used to detect the distribution of impurity metal,<sup>10,11</sup> and thiocyanate etching has been used to remove surface Pb species of CsPbBr<sub>3</sub> NCs to improve performance,<sup>12</sup> and acetone etching has been used to partially remove the surface iodine of CsPb(Br<sub>x</sub>I<sub>1-x</sub>)<sub>3</sub> NCs to form a stable bromine-rich surface.<sup>13</sup> Herein, the etching process caused by ODE and EA was used to evaluate the purification stability of CsPbBr<sub>2</sub> NCs, providing an intuitive and convenient method for characterizing the stability of the perovskite. Nevertheless, many obscure issues in the etching process are remaining, including the mechanism of the etching process, the influence of the antisolvent type and volume, whether the etching process will occur in CsPbX<sub>3</sub> (X=Cl or Br). Our research on the etching process highlights the important role of ODE and antisolvent EA, which could be used to modify and investigate the structure and evaluate the purification stability of PNCs.

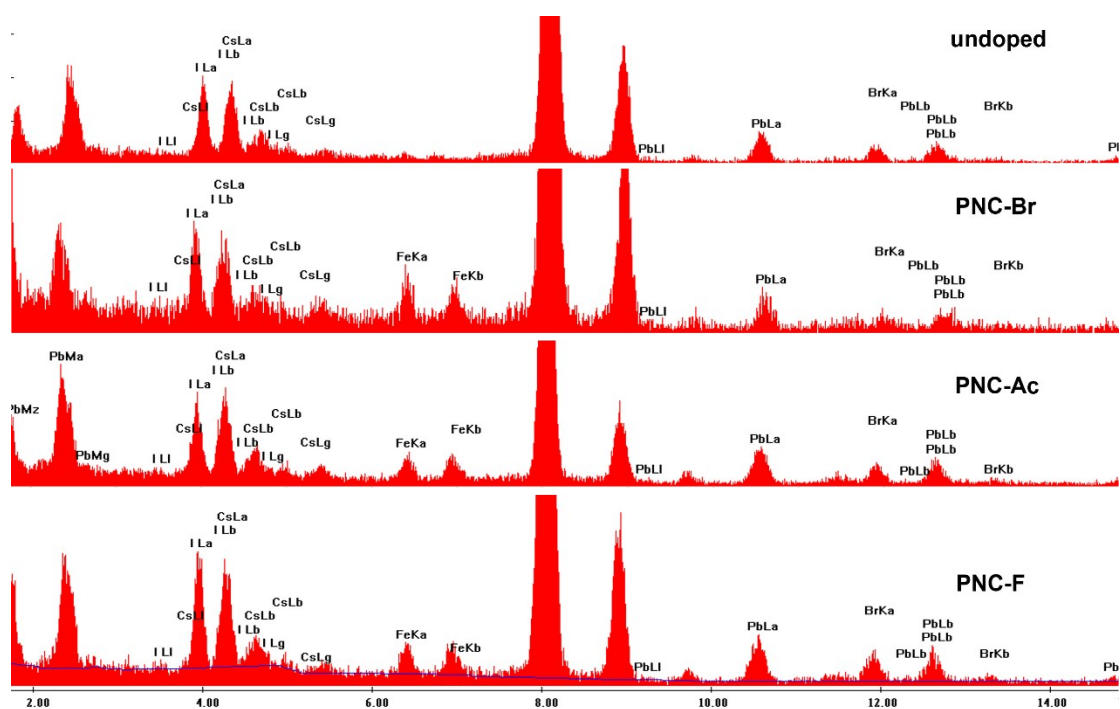


**Fig. S1** Energy dispersive X-ray spectroscopy (EDS) of undoped and  $\text{Fe}^{2+}$  doped  $\text{CsPbBr}_2$  NCs.

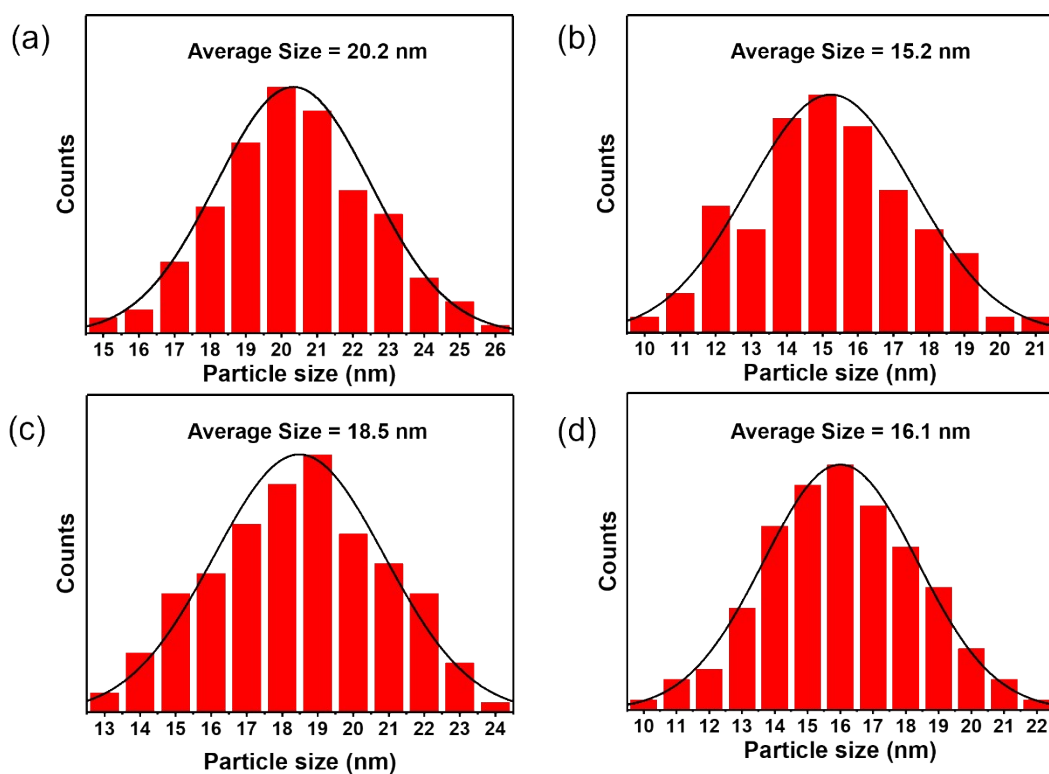


**Fig. S2** Particle size statistical charts of (a) undoped  $\text{CsPbBr}_2$  NCs, (b) Br-2.4%, (c) Ac-2.1%, (d) F-1.7%.

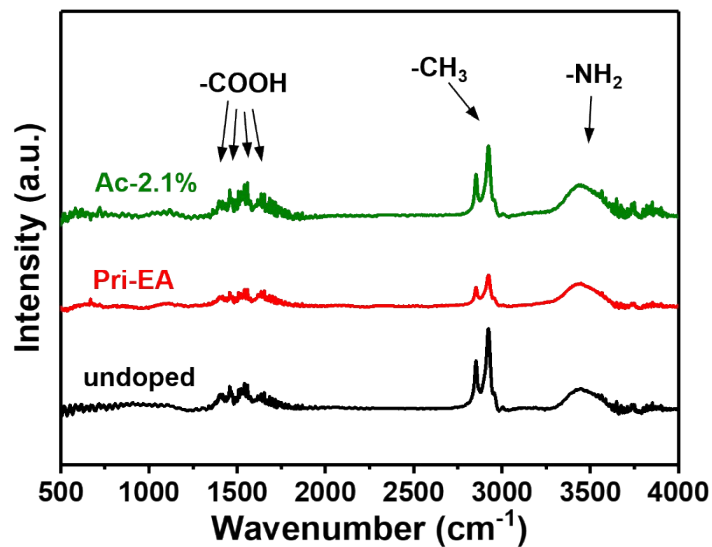


**Fig. S3** FTIR of undoped CsPbBr<sub>2</sub> NCs, Pri-EA and Ac-2.1%.

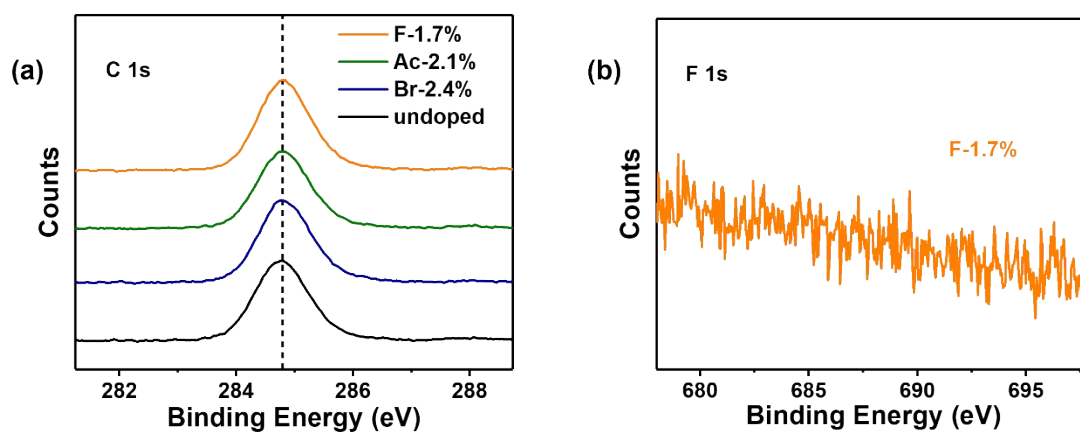


**Fig. S4** (a) XPS C 1s spectra of corresponding samples after peak calibration at 284.80 eV. (b) XPS F 1s spectra of F-1.7%.

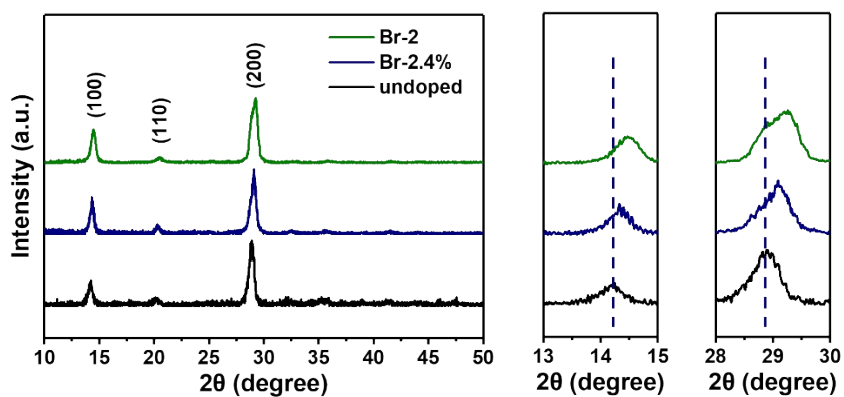


**Fig. S5** XRD pattern of undoped CsPbBr<sub>2</sub> NCs, Br-2.4%, and Br-2. Enlarged XRD patterns show a systematic shift in peak position of (100) and (200) planes with the increasing of Fe<sup>2+</sup> content.

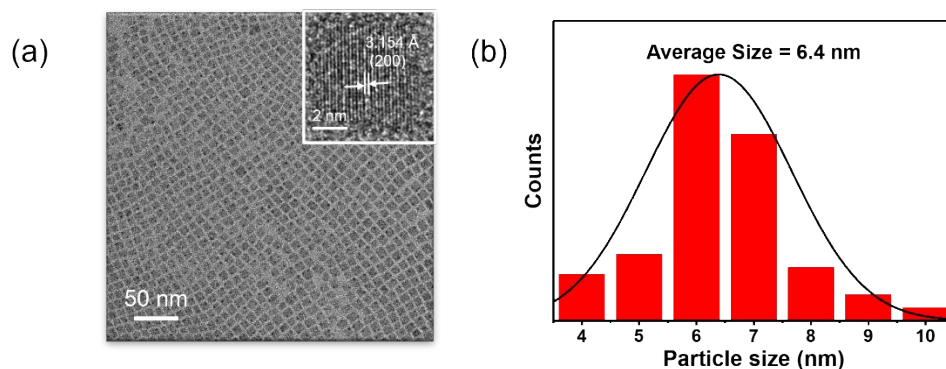


**Fig. S6** (a) TEM and HR-TEM images of Br-2, and (b) corresponding particle size statistical chart. (c) Steady state absorption (dotted line) and PL (solid line) spectra of Br-2. Inset shows the photographs of Br-2 in hexane under UV-light (365 nm) irradiation.

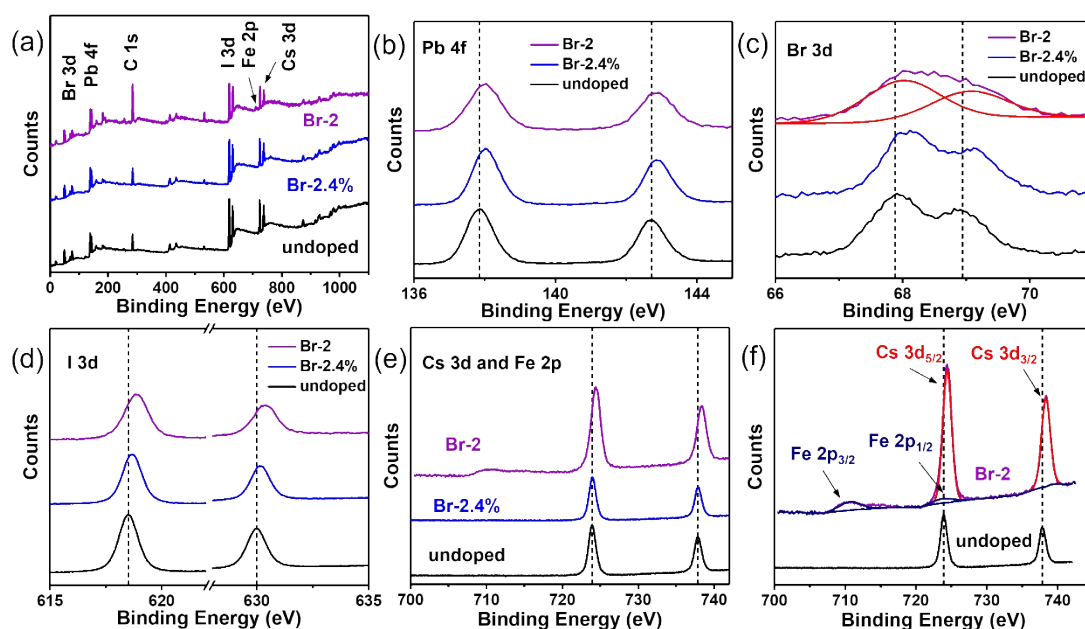


**Fig. S7** (a) Survey XPS spectra and (b-e) HR-XPS spectrum of Pb, Br I, Cs and Fe for undoped CsPbBr<sub>2</sub> NCs, Br-2.4% and Br-2. (f) Fitting curves of HR-XPS spectrum of Cs 3d and Fe 2p for Br-2.

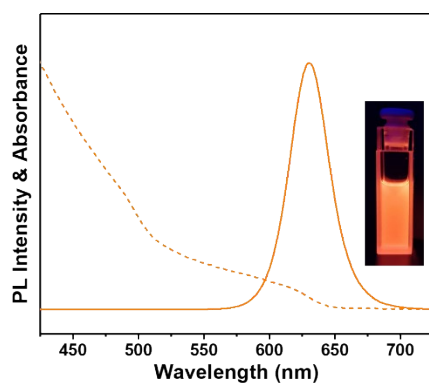


**Fig. S8** Steady state absorption (dotted line) and PL (solid line) spectra of Br-2. Inset shows the photographs of Br-2 in hexane under UV-light (365 nm) irradiation.

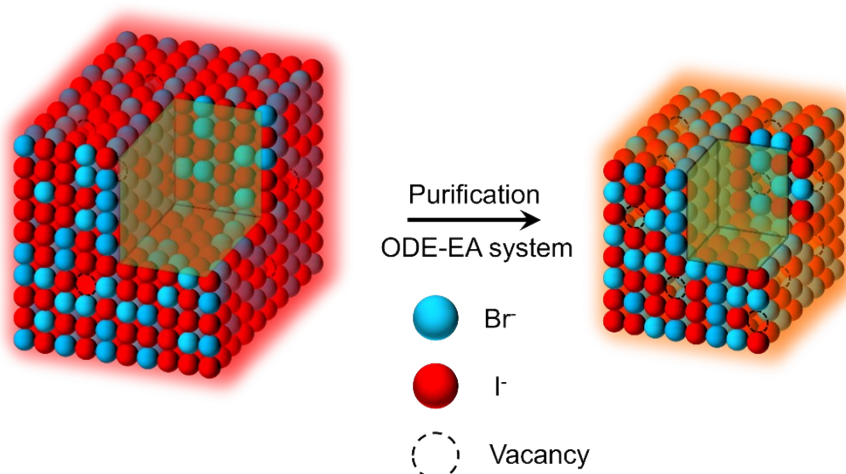


**Fig. S9** Schematic illustration showing the structural changes after the surface etching process. The surface structure of PNC is destroyed by ODE and EA, and halide ion vacancies are generated during this process.

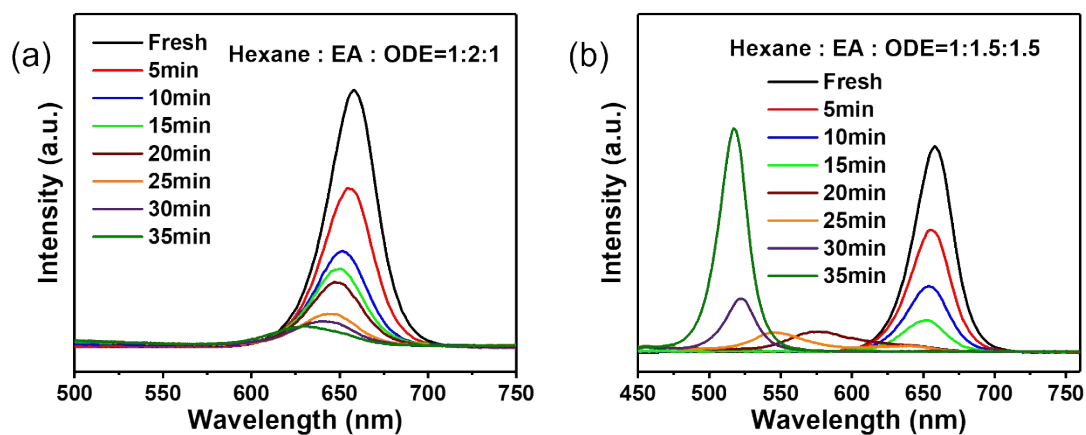


**Fig. S10** The time-dependent PL spectrum of CsPbBr<sub>2</sub> NCs solution by adding mixed solvent (3 mL) containing ODE and EA with a volume ratio of (a) 1:2 and (b) 1:1 to 1 mL NCs suspension (in hexane).

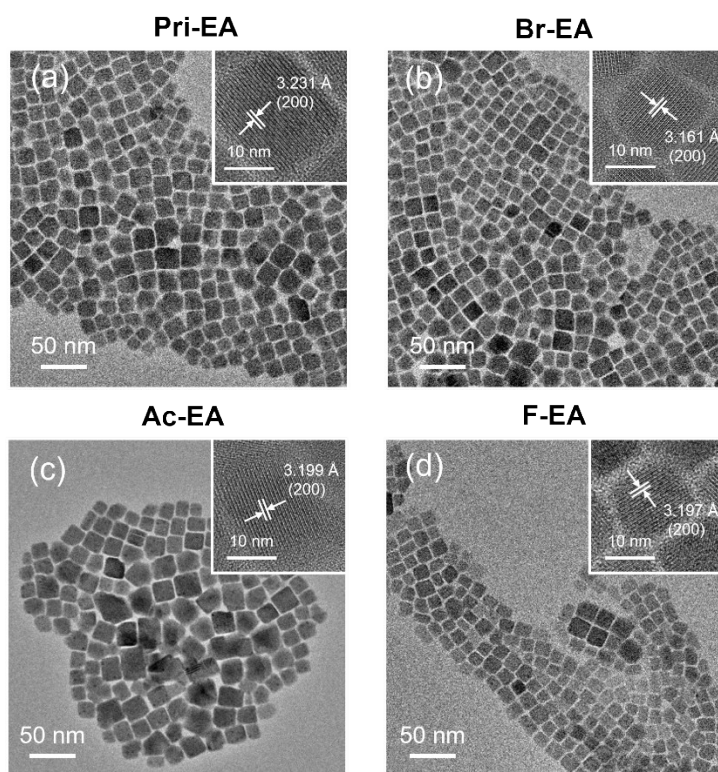


**Fig. S11** TEM and HR-TEM images of Pri-EA (a), Br-EA (b), Ac-EA (c), F-EA (d).

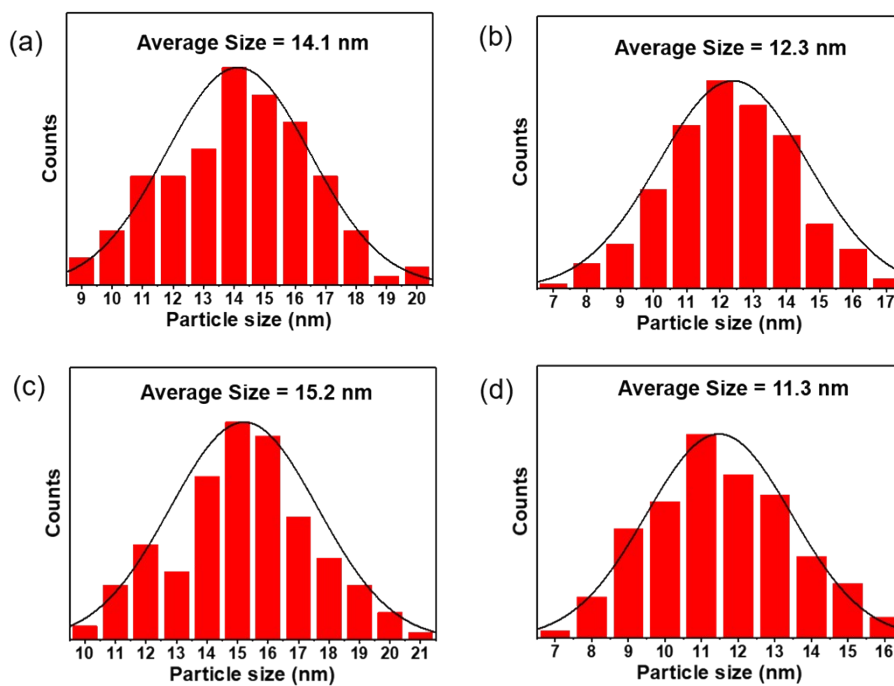


**Fig. S12** Particle size statistical charts of Pri-EA (a), Br-EA (b), Ac-EA (c), F-EA (d).

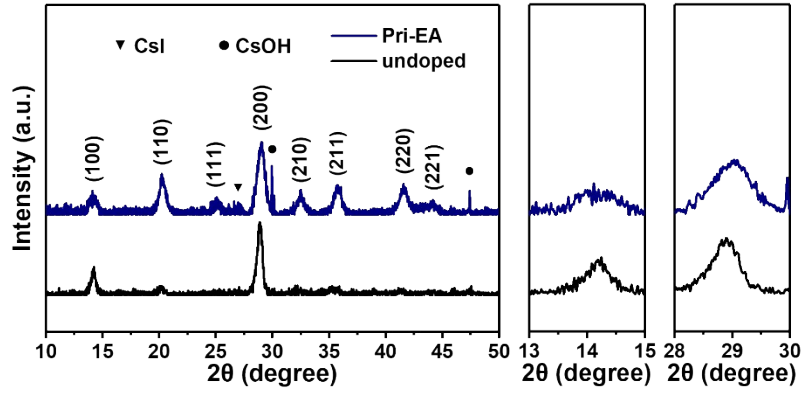


**Fig. S13** XRD pattern of undoped CsPbBr<sub>2</sub> NCs and Pri-EA film.

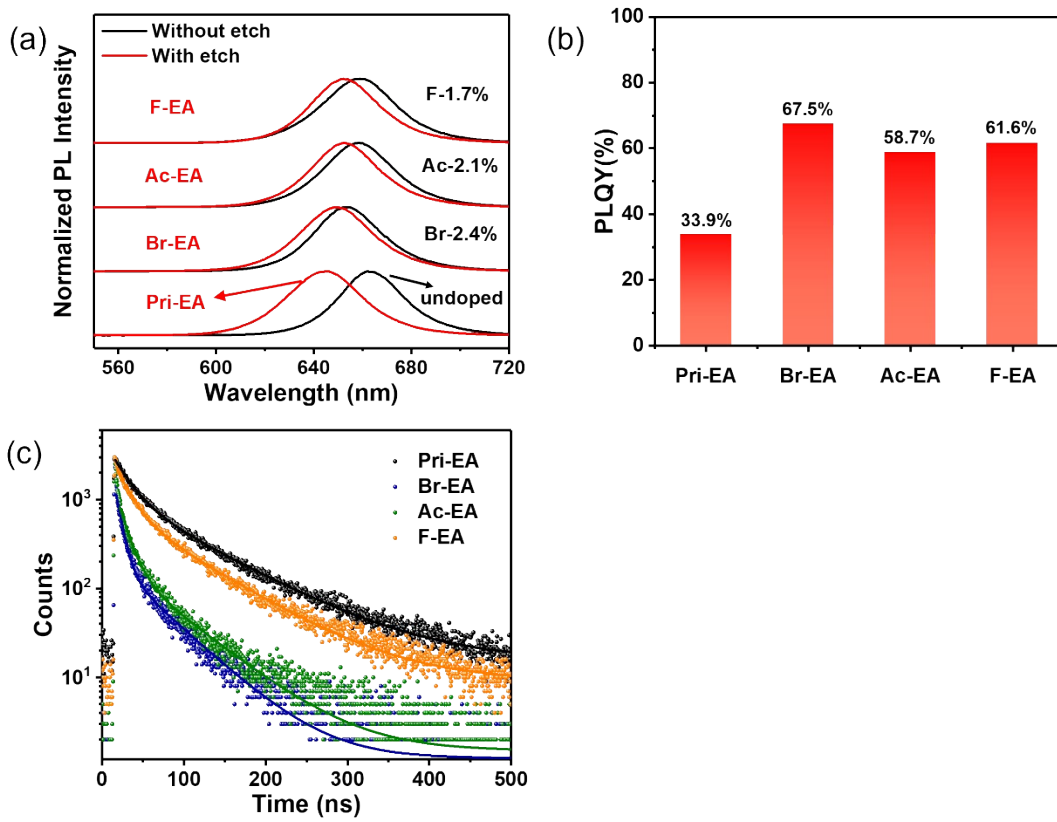


**Fig. S14** (a) The PL spectrum of obtained PNCs using different centrifugal method. The black and red lines correspond to the samples obtained using centrifugal method 1 and 2, respectively. (b) The PLQY values of Pri-EA, Br-EA, Ac-EA, F-EA. (c) Time-resolved photoluminescence decays for excitonic luminescence of PNC-EA upon excitation by a 375-nm pulsed laser.

**Table S1.** Amounts of  $\text{PbBr}_2$ ,  $\text{PbI}_2$  and iron precursor added for undoped  $\text{CsPbBrI}_2$  NCs and  $\text{Fe}^{2+}$  doped  $\text{CsPbBrI}_2$  NCs.

Sample	$\text{PbBr}_2$	$\text{PbI}_2$	Iron precursor
undoped	48.8 mg (0.133mmol)	123.6 mg (0.267 mmol)	
PNC-Br		185.2 mg (0.4 mmol)	$\text{FeBr}_2$ (43.1 mg, 0.2 mmol)
PNC-Ac	0.133mmol	0.267 mmol	$\text{FeAc}_2$ (34.8 mg, 0.2 mmol)
PNC-F	0.133mmol	0.267 mmol	$\text{FeF}_2$ (18.8 mg, 0.2 mmol)
Br-2	0.133mmol	0.267 mmol	$\text{FeBr}_2$ (57.6 mg, 0.267 mmol) $\text{FeI}_2$ (165.0 mg, 0.533 mmol)

**Table S2.** The calculated values of quantum confinement energy ( $\Delta E$ ), quantum confinement energy difference ( $\Delta E_{\text{cal}}$ ), PL energy difference ( $\Delta E_{\text{PL}}$ ).

Sample	$\Delta E$ ( $\times 10^{-3}$ eV)	$\Delta E_{\text{cal}}$ ( $\times 10^{-3}$ eV)	$\Delta E_{\text{PL}}$ ( $\times 10^{-3}$ eV)
undoped	6.19		
Br-2.4%	10.96	4.77	22.33
Ac-2.1%	7.39	1.20	10.82
F-1.7%	9.79	3.60	9.67

**Table S3.** The table encloses PL lifetimes, PLQY values, radiative ( $K_r$ ) and nonradiative ( $K_{nr}$ ) decay rates of undoped PNCs, Br-2.4%, Ac-2.1%, F-1.7%. The values in the parentheses of  $\tau_1$  and  $\tau_2$  represent the statistical weights of the corresponding lifetime components.

Samples	undoped	Br-2.4%	Ac-2.1%	F-1.7%
$\tau_1$ (ns)	31.5 (24.5%)	24.0 (65.5%)	26.2 (54.7%)	28.1 (31.6%)
$\tau_2$ (ns)	152.2 (75.5%)	89.5 (34.5%)	87.5 (45.3%)	100.5 (68.4%)

$\tau_{av}$ (ns)	144.6	67.4	71.2	92.2
PLQY (%)	69.2	92.1	89.3	87.6
$K_r$ ( $\times 10^6$ s $^{-1}$ )	4.784	13.65	12.53	9.499
$K_{nr}$ ( $\times 10^6$ s $^{-1}$ )	2.129	1.171	1.502	1.345

**Table S4.** The table encloses the PL peak position ( $\lambda_{PL}$ ), PL lifetimes, PLQY values, radiative ( $K_r$ ) and nonradiative ( $K_{nr}$ ) decay rates of Pri-EA, Br-EA, Ac-EA, F-EA. The values in the parentheses of  $\tau_1$  and  $\tau_2$  represent the statistical weights of the corresponding lifetime components.

Samples	Pri-EA	Br-EA	Ac-EA	F-EA
$\lambda_{PL}$ (nm)	642.9	649.5	653.0	652.9
$\tau_1$ (ns)	20.4 (28.4%)	7.4 (46.3%)	11.7 (43.0%)	17.0 (32.7%)
$\tau_2$ (ns)	86.4 (71.6%)	50.9 (53.7%)	59.7 (57.0%)	76.6 (67.3%)
$\tau_{av}$ (ns)	80.7	46.0	53.5	70.8
PLQY (%)	33.9	67.5	58.7	61.6
$K_r$ ( $\times 10^6$ s $^{-1}$ )	4.198	14.65	10.97	8.696
$K_{nr}$ ( $\times 10^6$ s $^{-1}$ )	8.185	7.056	7.719	5.421

**Table S5.** The size change, shift of PL peak position, and PLQYs of the synthesized PNCs using centrifugation methods 1 and 2. PLQY-1 and PLQY-2 represent the PLQY values of the samples obtained using centrifugation methods 1 and 2, respectively.

Samples	Pri-EA	Br-EA	Ac-EA	F-EA
$ \Delta \text{size} $ (nm)	6.1	2.9	3.3	4.8

$ \Delta \lambda_{PL} $ (nm)	19.1	4.8	5.4	5.6
PLQY-1	69.2%	92.1%	89.3%	87.6%
PLQY-2	33.9%	67.5%	58.7%	61.6%

---

## References

- 1 G. M. Dalpian and J. R. Chelikowsky, *Phys. Rev. Lett.*, 2006, **96**, 226802.
- 2 A. K. Jena, A. Kulkarni, Y. Sanehira, M. Ikegami and T. Miyasaka, *Chem. Mater.*, 2018, **30**, 6668-6674.
- 3 C. M. Guvenc, Y. Yalcinkaya, S. Ozen, H. Sahin and M. M. Demir, *J. Phys. Chem. C*, 2019, **123**, 24865-24872.
- 4 Y. Zhang, T. D. Siegler, C. J. Thomas, M. K. Abney, T. Shah, A. De Gorostiza, R. M. Greene and B. A. Korgel, *Chem. Mater.*, 2020, **32**, 5410-5423.
- 5 A. R. M. Abhishek Swarnkar, Erin M. Sanehira, Boris D. Chernomordik, David T. Moore, Jeffrey A. Christians, Tamoghna Chakrabarti, Joseph M. Luther, *Science*, 2016, **354**, 92-95.
- 6 Y. Kim, E. Yassitepe, O. Voznyy, R. Comin, G. Walters, X. Gong, P. Kanjanaboos, A. F. Nogueira and E. H. Sargent, *ACS Appl. Mater. Interfaces*, 2015, **7**, 25007-25013.
- 7 I. C. Smith, E. T. Hoke, D. Solis-Ibarra, M. D. McGehee and H. I. Karunadasa, *Angew. Chem. Int. Ed. Engl.*, 2014, **53**, 11232-11235.
- 8 J. Zhang, L. Zhang, P. Cai, X. Xue, M. Wang, J. Zhang and G. Tu, *Nano Energy*, 2019, **62**, 434-441.
- 9 M. Yamauchi, Y. Fujiwara and S. Masuo, *ACS Omega*, 2020, **5**, 14370-14375.
- 10 J.-K. Chen, J.-P. Ma, S.-Q. Guo, Y.-M. Chen, Q. Zhao, B.-B. Zhang, Z.-Y. Li, Y. Zhou, J. Hou, Y. Kuroiwa, C. Moriyoshi, O. M. Bakr, J. Zhang and H.-T. Sun, *Chem. Mater.*, 2019, **31**, 3974-3983.
- 11 J. Lu, S.-C. Chen and Q. Zheng, *Sci. China Chem.*, 2019, **62**, 1044-1050.
- 12 B. A. Koscher, Z. Nett and A. P. Alivisatos, *ACS Nano*, 2019, **13**, 11825-11833.
- 13 Q. Jing, M. Zhang, X. Huang, X. Ren, P. Wang and Z. Lu, *Nanoscale*, 2017, **9**, 7391-7396.